nature materials

LETTERS

https://doi.org/10.1038/s41563-019-0303-x

A gap-protected zero-Hall effect state in the quantum limit of the non-symmorphic metal KHgSb

Sihang Liang[1], Satya Kushwaha[2], Tong Gao[1], Max Hirschberger[1], Jian Li[1,4], Zhijun Wang[1], Karoline Stolze[2], Brian Skinner[3], B. A. Bernevig[1], R. J. Cava[2] and N. P. Ong[1*]

A recurring theme in topological matter is the protection of unusual electronic states by symmetry, for example, protection of the surface states in Z_2 topological insulators by time-reversal symmetry[1–3]. Recently, interest has turned to unusual surface states in the large class of non-symmorphic materials[4–12]. In particular, KHgSb is predicted to exhibit double quantum spin Hall states[10]. Here we report measurements of the Hall conductivity in KHgSb in a strong magnetic field *B*. In the quantum limit, the Hall conductivity is observed to fall exponentially to zero, but the diagonal conductivity is finite. A large gap protects this unusual zero-Hall state. We theoretically propose that, in this quantum limit, the chemical potential drops into the bulk gap, intersecting equal numbers of right- and left-moving quantum spin Hall surface modes to produce the zero-Hall state. The zero-Hall state illustrates how topological protection in a non-symmorphic material with glide symmetry may lead to highly unusual transport phenomena.

KHgSb crystallizes in the non-symmorphic space group $D_{6h}^4(P6_3/mmc)$. The Hg and Sb ions define honeycomb layers with *AB* stacking (Fig. 1a)[10]. The combination of strong spin–orbit coupling, inversion symmetry and band inversion leads to non-trivial topological properties (Supplementary Section 1). As the mirror Chern number $\mathcal{C}_M = 2$, we have double quantum spin Hall (QSH) states (two left- and two right-moving modes) on each of the surfaces (100) and (010). The QSH states disperse along the blue lines in the inset in Fig. 1a, with velocity $\mathbf{v}_g \,||\, \mathbf{x}$ or $\mathbf{y}$. At their intersections, left- and right-moving QSH states are protected against hybridization by mirror symmetry across the mirror plane M_z.

Crystals of KHgSb grow as plates with the broad faces normal to $\hat{\mathbf{z}}||[001]$, and side faces identified with (100) and (010). Hall measurements in a field $\mathbf{B}||\mathbf{z}$ with current in the *x*–*y* plane can detect the QSH states, provided the chemical potential μ lies inside the bulk gap. (Our measurements do not couple to the hourglass modes[13,14] because they disperse along $\widetilde{\Gamma}\widetilde{Z}$ with $\mathbf{v}_g||\mathbf{z}$.)

We report results from two batches of crystals (Supplementary Sections 2 and 3 and Supplementary Table 1). In batch A (nominally undoped), Hg vacancies lead to a carrier density (*n*-type) $n \sim 9.5 \times 10^{17}\,\mathrm{cm}^{-3}$ (determined from the weak-*B* Hall effect). In batch B, Bi dopants were added to reduce *n* by a factor of 4. In both batches, μ lies low in the conduction band when $B = 0$. In batch A, the in-plane resistivity ρ_a ($B = 0$) is nearly independent of temperature *T*, with a mobility $\mu_e \sim 3{,}500\,\mathrm{cm}^2\,\mathrm{V}^{-1}\,\mathrm{s}^{-1}$ limited by dominant impurity scattering (Supplementary Fig. 1). In batch B, ρ_a increases by 30–40% between 40 and 4 K. (The sharp downturns at 4 K in Supplementary Fig. 1 are caused by trace superconductivity from exuded Hg ions at the crystal surface; they do not affect the conclusions.) Batch A crystals display strong Shubnikov de Haas (SdH) oscillations. In Fig. 1b, SdH oscillations in the resistivity ρ_{xx} (with $\mathbf{B}||\mathbf{z}$) are plotted at selected *T*. At the field B_{QL} at which ρ_{xx} has a deep minimum, μ enters the lowest Landau level (LLL). From the damping of the SdH amplitudes versus *T* we infer a small in-plane mass $m_a = 0.05 m_e$ (m_e is the free electron mass). The Fermi surface is highly elongated along $\mathbf{z}$, implying a weak interlayer coupling (Supplementary Section 6 and Supplementary Fig. 10).

A hint of interesting behaviour in the LLL was first detected in the field profiles of the Hall angle $\tan\theta_H$ (Fig. 1c). Whereas $\tan\theta_H$ is *B*-linear and *T* independent below 5 T, it varies strongly with *B* and *T* once μ enters the LLL (the peak occurs at B_{QL}). Further hints emerged from the *T* dependencies of the resistivity ρ_{xx} and Hall resistivity ρ_{yx} in intense $\mathbf{B}||\mathbf{z}$ (Fig. 1d). The prominent increase in ρ_{xx} in a 63-T field (60-fold at 2 K) suggests a dramatic loss of carriers, which should cause the Hall resistivity ρ_{yx} to diverge. Paradoxically, we find instead that ρ_{yx} measured with *B* fixed at 62.5 T (red circles) plunges steeply to 0 below ~40 K.

To understand these features, we turn to the field profiles in Fig. 2 measured at low *T* with $\mathbf{B}||\mathbf{z}$. Using pulsed fields, we extended measurements of the resistivity ρ_{xx} to 63 T, well beyond $B_{QL} \sim 11$ T (Fig. 2a). Whereas ρ_{xx} is relatively flat below B_{QL} (aside from the SdH oscillations), it shows a steep 60-fold increase above B_{QL} (see curve at 1.53 K), consistent with a sharp decrease in the carrier density *n*, as noted above. However, above 45 T, ρ_{xx} bends over to approach saturation instead of continuing to diverge.

Simultaneously, the Hall resistivity ρ_{yx} displays a striking field profile (Fig. 2b). At the lowest *T* (1.53 K), ρ_{yx} deviates sharply at B_{QL} from the usual *B*-linear Hall dependence, describes a broad maximum and then plunges steeply to 0 above 45 T, where it remains pinned up to the highest $B = 63$ T. As we raise *T* from 1.5 to 10 K, the high-field curves of ρ_{yx} strongly deviate from 0 in a thermally activated way that defines an energy gap (Supplementary Figs. 1–4).

In intense fields, it is best to analyse the Hall conductivity σ_{xy}. Inverting the matrix ρ_{ij}, we obtain the curves of $\sigma_{xy}(B)$ (Fig. 2c). At 150 K, the measured σ_{xy} closely follows the semiclassical form (shown as the dashed curve)

$$\sigma_{xy} = ne\mu_e^2 B \,/\, [1 + \mu_e^2 B^2] \qquad (1)$$

with *n* being the carrier density in the LLL and *e* being the charge. With $\mu_e = 3{,}500\,\mathrm{cm}^2\,\mathrm{V}^{-1}\,\mathrm{s}^{-1}$, we have $\sigma_{xy} \to ne/B$ for $B > 20$ T; that is, σ_{xy} depends only on *n* because dissipation effects (μ_e) cancel out.

[1]Department of Physics, Princeton University, Princeton, NJ, USA. [2]Department of Chemistry, Princeton University, Princeton, NJ, USA. [3]Department of Physics, Massachusetts Institute of Technology, Cambridge, MA, USA. [4]Present address: School of Science, Westlake University, Hangzhou, China. *e-mail: npo@princeton.edu

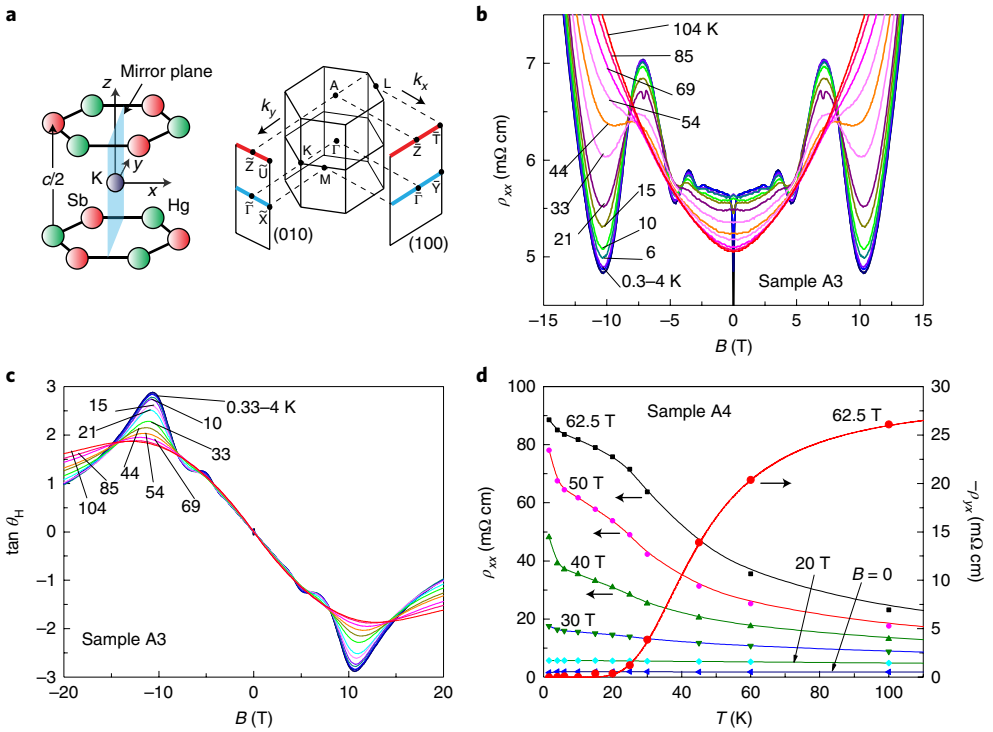

Fig. 1 | The quantum limit in KHgSb. a, The crystal structure of KHgSb and the bulk and surface Brillouin zones. The blue and red lines are mirror planes $\overline{M}_z$ at wavevector $k_z = 0, \pi/c$ (c is the lattice parameter). **b**, The SdH oscillations for $0.3 < T < 104$ K (sample A3, magnetic field **B**||**z**). Indexing the oscillations reveals that the chemical potential μ enters the LLL at the deep minimum near 10 T. Damping of the SdH amplitudes yields an in-plane mass $m_a = 0.05$ m_e (m_e is the free mass). **c**, The field profiles of the Hall angle tan θ_H at selected T (in A3). At the peak (~11 T), μ enters the LLL. **d**, Divergent behaviours of the Hall resistivity ρ_{yx} (red circles) and resistivity ρ_{xx} (symbols) in the LLL. As $T \to 2$ K, ρ_{xx} increases steeply, implying a sharp decrease of the itinerant population. Paradoxically, the Hall resistivity ρ_{yx} (a negative quantity) plunges to 0 below 20 K instead of diverging to very large values as expected from loss of itinerant carriers. These opposite trends imply a surface conduction channel in parallel with the bulk (see text). The saturation of ρ_{xx} at 62 T as $T \to 2$ K also constitutes evidence for the surface conduction mode. The solid red curve is a fit to ρ_{yx} using equation (1); the curves drawn through the ρ_{xx} symbols are guides to the eye.

The key observation is that $\sigma_{xy}(T, B)$ becomes strongly T dependent once B exceeds an onset field $B_c \sim 22$ T (arrow in Fig. 2c). The strong T dependence is well described by $n(T,B) = n_0 e^{-\Delta(B)/k_B T}$ with a B-dependent gap $\Delta(B)$ (k_B is Boltzmann's constant). The close fits of σ_{xy} are shown magnified in Fig. 2d. (At each B, $\Delta(B)$ is uniquely obtained from the Arrhenius plot of σ_{xy} with the prefactor $n_0 = 9.5 \times 10^{17}$ cm^{-3}. The gap values are plotted in the inset in Fig. 2c.) We stress that, above 20 T, σ_{xy} depends only on $n(T, B)$ because the mobility μ_e cancels out. The activated behaviour in $n(T, B)$ ensures that σ_{xy} is pinned to zero in the limit $\Delta(B)/k_B T \gg 1$.

In our analysis, the conductivity σ_{xx} initially increases with field just above B_{QL} reflecting the increasing density of states (Supplementary Section 8). However, above B_c, σ_{xx} falls steeply, and asymptotes to a B- and T-independent constant σ^S which we identify with surface modes. In the 7 batch A samples, σ^S varies from 2.5 to 40 $(\Omega\ \text{cm})^{-1}$ (or 0.03 and $0.1e^2/h$ per HgSb layer). As emphasized above, the surface mode displays zero Hall response. The finite σ^S explains why $\rho_{yx} \to 0$ rather than ∞ in the limit $n \to 0$.

We also observe the zero-Hall state in samples B1 and B3. Figure 3a displays curves of ρ_{yx} measured in sample B3 (where $B_{QL} \sim 3$ T, instead of 12 T). At 2 K, ρ_{yx} approaches 0 as an activated form when $B > 10$ T. The gap $\Delta(B)$ inferred from the semilog plot of σ_{yx} versus $1/T$ (Fig. 3c) is plotted in the inset in Fig. 3a. As shown in Fig. 3c, the zero-Hall state survives to large field-tilt angles θ (see scaling plot in Supplementary Fig. 11). The similarity of the profiles of ρ_{yx} in A4 (Fig. 2b) and B3 (Fig. 3b) implies that the zero-Hall state is intrinsic to the LLL (when $B > B_{QL}$). The large resistivity anisotropy ($\rho_{zz}/\rho_{xx} \sim 270$; Supplementary Section 5 and Supplementary Fig. 9), together with the highly elongated Fermi surface, implies a very weak interlayer hopping, consistent with dominant conduction via σ^S.

Ab initio calculations reveal the special status of the LLL (Fig. 4, Supplementary Section 7 and Supplementary Fig. 12). In intense B (60 T), the LLL in the conduction band and its partner level (at energies $E_0 = 0.18$ and $E_0' = 0.35$ eV, respectively) disperse downwards at the sample's edge, reflecting their hole-state origin (Fig. 4b). Together, these two edge states constitute the left-moving QSH modes. Conversely, a pair of right-moving QSH modes arise from the LL at the valence band maximum. Hence, there exist two left- and two right-moving QSH modes. All four modes intersect μ if it lies in the bulk gap (solid line in Fig. 4b). By Büttiker–Landauer theory[15,16], we must have $\sigma_{xy} = 0$, but σ_{xx} will remain finite.

As noted, the disparate behaviours of σ_{xy} and σ_{xx} in the quantum limit suggest parallel conduction channels by bulk carriers and surface modes. In a conventional clean semimetal, μ is pinned at E_0 in the quantum limit (dashed line in Fig. 4b). However, if μ drops into the gap (that is, itinerant bulk carriers vanish), the Büttiker–Landauer theory should apply. One mechanism that produces such a downward shift in μ (as well as thermal activation in $n(T)$) is magnetic freeze-out, long familiar in bulk semiconductors[17–19] (Supplementary Section 8 and Supplementary Fig. 13). Whereas the electrons are unbound in zero B, a strong B deepens the binding energy to donors (Hg vacancies). At the field

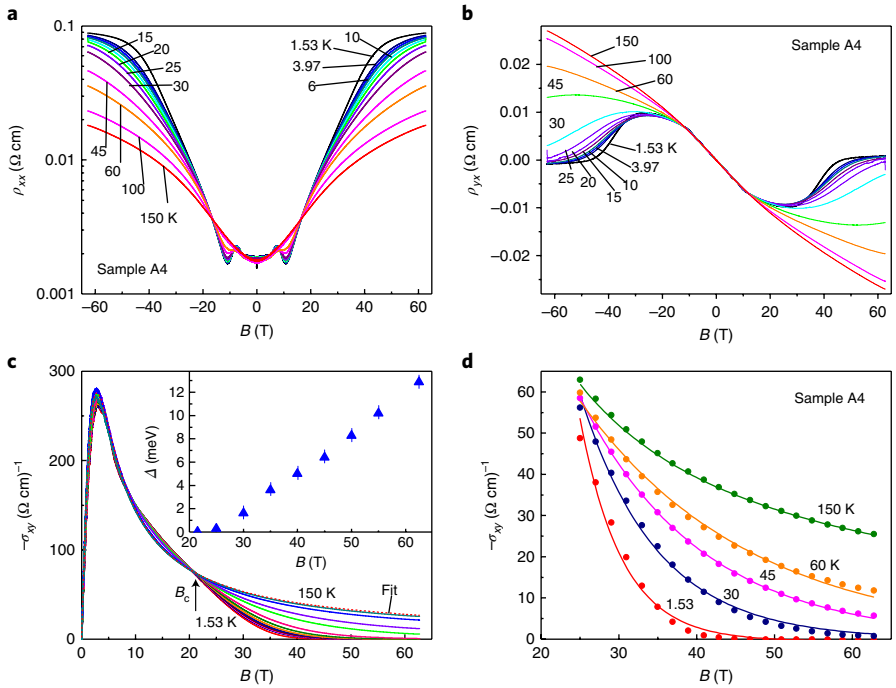

Fig. 2 | Emergence of a zero-Hall state and gap in sample A4. a, Curves of ρ_{xx} versus B for selected temperatures T (semilog scale). At fields $B > \sim 11$ T, ρ_{xx} at 1.53 K increases steeply, but saturates above 60 T. **b**, The Hall resistivity curves ρ_{yx} versus B. Below 100 K, ρ_{yx} displays strong T dependence when μ enters the LLL. When B exceeds ~35 T, ρ_{yx} falls steeply, consistent with thermal activation across a gap $\Delta(B)$. **c**, Curves of the Hall conductivity σ_{xy} versus B at selected T (given in **b**). The red dashed curve is the fit to equation (1) with carrier density $n = n_0$ at 150 K. The strong T dependence that appears above the onset field $B_c \sim 22$ T (arrow) is well described by equation (1) with $n(T) = n_0 e^{-\Delta(B)/k_B T}$. The gap $\Delta(B)$ inferred from the fits increases to 13 meV at 62.5 T (inset). The vertical lines indicate the uncertainties in determining $\Delta(B)$ from the fits. **d**, Fits to equation (1) (solid curves) for fields $B_c < B < 63$ T at selected T. At 150 K we fix $n = n_0$, whereas at and below 60 K we use the thermally activated form for $n(T)$. In **c** and **d**, σ_{xy} is a negative quantity, like ρ_{yx}.

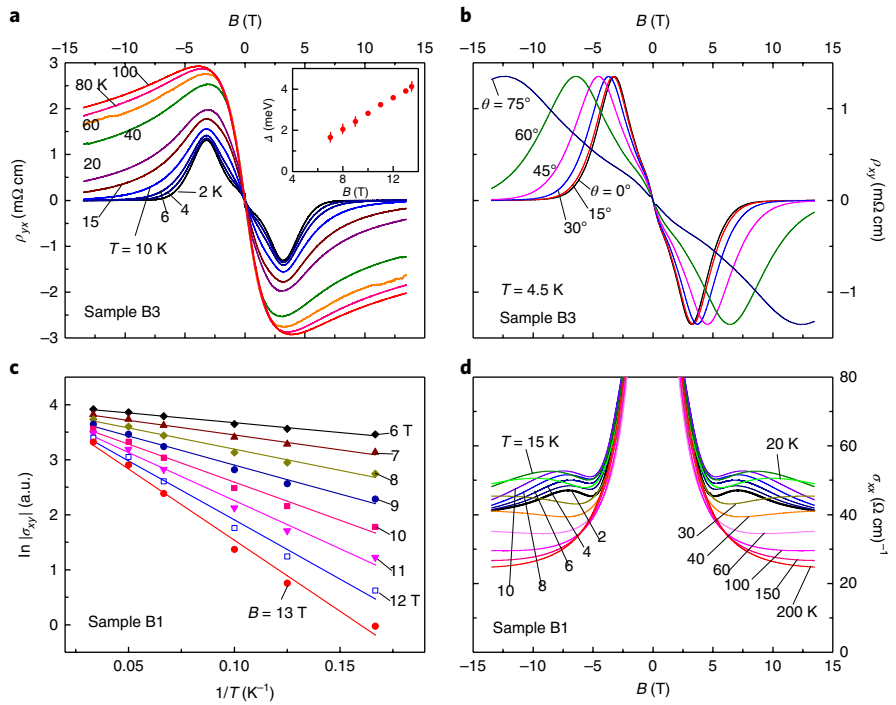

Fig. 3 | The zero-Hall state in Bi-doped KHgSb (batch B). a, Curves of the Hall resistivity ρ_{yx} in B3. The field profiles are similar to Fig. 2b except for the much lower field scales. The inferred gap Δ is plotted versus B in the inset (vertical lines are error bars). **b**, The effect of varying the tilt angle θ of **B** relative to **z** at 4.5 K. All of the curves at $\theta < 60°$ collapse to a universal curve when plotted against B_z (see Supplementary Fig. 11). **c**, Semilog plot of $|\sigma_{xy}|$ versus $1/T$ at selected B (in Sample B1). **d**, Curves of the conductivity σ_{xx} versus B for sample B1. At 2 K (black curve), $\sigma_{xx} \to 41\ (\Omega\ \mathrm{cm})^{-1}$ or ~$0.1e^2/h$ per mode above 10 T.

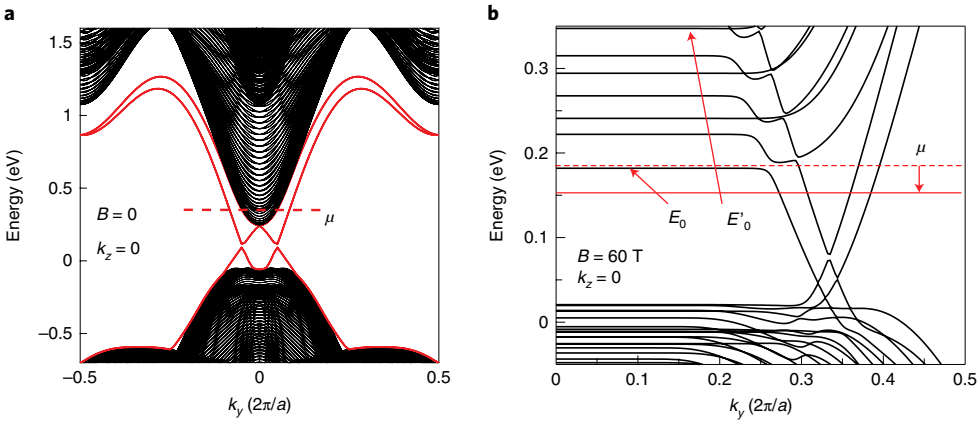

Fig. 4 | Ab initio band structure of KHgSb near Γ in $B = 0$ and in strong B. a, Direct gap of 320 meV separating the bulk states (black curves) in $B = 0$. Pairs of right- and left-moving QSH states (red curves) traverse the gap. **b**, The LL spectrum in $B = 60$ T with zigzag termination on a (100) surface. In the conduction band, all LLs disperse upwards at the surface except for the lowest LL (at energy $E_0 \sim 0.18$ eV) and its partner produced by band folding at $k_z = \pi/c$ at energy $E'_0 \sim 0.35$ eV, which disperse downwards to form a pair of left-moving QSH states. Conversely, a pair of right-moving QSH states emerge from the valence band. In the quantum limit, magnetic freeze-out lowers μ into the gap (dashed line to solid) where it intersects two left- and two right-moving QSH modes to give $\sigma_{xy} = 0$.

B_c, the binding energy becomes large enough to localize bulk carriers onto impurity states[17], so that μ falls below E_0 into the bulk gap (solid line in Fig. 4b). When $\Delta/k_BT \gg 1$, the itinerant bulk population is completely suppressed. The entire current is then carried by the four QSH modes, so that the zero-Hall state with finite σ_{xx} is realized.

We have considered whether a semiclassical three-band Drude model can explain our findings (details in Supplementary Section 9 and Supplementary Fig. 14). As discussed in Supplementary Section 9, the key features here—the sharp onset at B_c of thermal activation across a gap $\Delta(B)$ and pinning of σ_{xy} to zero up to 63 T—lie well beyond the purview of semiclassical transport (see especially the plots of $\sigma_{xy}(B)$ in Fig. 2c,d and Supplementary Fig. 15). Moreover, photoemission[13,14] and ab initio band calculations do not see three bands. In addition, we distinguish our results from the anomalous Hall effect[20] in ferromagnets and conventional semimetals (Supplementary Section 10).

In summary, the Hall conductivity σ_{xy} in KHgSb exhibits a remarkable exponential decrease to zero when the chemical potential μ enters the LLL in the quantum limit. The activated behaviour of σ_{xy} yields an energy gap that appears abruptly at the onset field B_c. The gap pins σ_{xy} to zero over an extended range of fields $B > B_c$. In contrast, the diagonal conductivity σ_{xx} remains finite. By varying the carrier density, we verified that the zero-Hall state occurs within the LLL, and is insensitive to tilting of **B**. We interpret the activation as caused by magnetic freeze-out, which describes field-induced trapping of the itinerant bulk carriers by Hg vacancies. As a consequence, μ is lowered into the bulk energy gap. The applied current is then conducted solely by the surface double QSH states predicted to exist in this non-symmorphic material. The counter-propagating double QSH states lead to the unusual gap-protected, zero-Hall state observed in the experiment.

Online content

Any methods, additional references, Nature Research reporting summaries, source data, statements of data availability and associated accession codes are available at https://doi.org/10.1038/s41563-019-0303-x.

Received: 19 September 2017; Accepted: 30 January 2019;
Published online: 4 March 2019

References

1. Fu, L., Kane, C. L. & Mele, E. H. Topological insulators in three dimensions. *Phys. Rev. Lett.* **98**, 106803 (2007).
2. Fu, L. & Kane, C. L. Topological insulators with inversion symmetry. *Phys. Rev. B* **76**, 045302 (2007).
3. Qi, X. L., Hughes, T. L. & Zhang, S. C. Topological field theory of time-reversal invariant insulators. *Phys. Rev. B* **78**, 195424 (2008).
4. Parameswaran, S. A. et al. Topological order and absence of band insulators at integer filling in non-symmorphic crystals. *Nat. Phys.* **9**, 299–303 (2013).
5. Liu, C. X., Zhang, R. X. & VanLeeuwen, B. K. Topological nonsymmorphic crystalline insulators. *Phys. Rev. B* **90**, 085304 (2014).
6. Shiozaki, K. & Sato, M. Topology of crystalline insulators and superconductors. *Phys. Rev. B* **90**, 165114 (2014).
7. Young, S. M. & Kane, C. L. Dirac semimetals in two dimensions. *Phys. Rev. Lett.* **115**, 126803 (2015).
8. Fang, C. & Fu, L. New classes of three-dimensional topological crystalline insulators: nonsymmorphic and magnetic. *Phys. Rev. B* **91**, 161105 (2015).
9. Shiozaki, K., Sato, M. & Gomi, K. Z_2 topology in nonsymmorphic crystalline insulators: Möbius twist in surface states. *Phys. Rev. B* **91**, 155120 (2015).
10. Wang, Z. J., Alexandradinata, A., Cava, R. J. & Bernevig, B. A. Hourglass fermions. *Nature* **532**, 189–194 (2016).
11. Schoop, L. M. et al. Dirac cone protected by non-symmorphic symmetry and three-dimensional Dirac line node in ZrSiS. *Nat. Commun.* **7**, 11696 (2016).
12. Wieder, B. J. et al. Wallpaper fermions and the nonsymmorphic Dirac insulator. *Science* **361**, 246–251 (2018).
13. Ma, J. et al. Experimental evidence of hourglass fermion in the candidate nonsymmorphic topological insulator KHgSb. *Sci. Adv.* **3**, e1602415 (2017).
14. Liang, A. J. et al. Observation of the topological surface state in the nonsymmorphic topological insulator KHgSb. *Phys. Rev. B* **96**, 165143 (2017).
15. Büttiker, M. Absence of backscattering in the quantum Hall effect in multiprobe conductors. *Phys. Rev. B* **38**, 9375–9389 (1988).
16. Beenakker, C. W. J. & van Houten, H. Quantum transport in semiconductor nanostructures. *Solid State Phys.* **44**, 1–228 (1991).
17. Dyakonov, M. I., Efros, A. L. & Mitchell, D. L. Magnetic freeze-out of electrons in extrinsic semiconductors. *Phys. Rev.* **180**, 813–818 (1969).
18. Goldman, V. J., Shayegan, M. & Drew, H. D. Anomalous Hall effect below the magnetic-field-induced metal-insulator transition in narrow-gap semiconductors. *Phys. Rev. Lett.* **57**, 1056–1059 (1986).
19. Mani, R. G. Influence of localization on the Hall effect in narrow-gap, bulk semiconductors. *Phys. Rev. B* **41**, 7922–7925 (1990).
20. Nagaosa, N., Sinova, J., Onoda, S., MacDonald, A. H. & Ong, N. P. Anomalous Hall effect. *Rev. Mod. Phys.* **82**, 1539–1592 (2010).

Acknowledgements

The research was supported by the Department of Energy (DE-SC0017863) and the Gordon and Betty Moore Foundation's EPiQS initiative through grants GBMF4539 (to N.P.O.) and GBMF-4412 (to R.J.C.). The crystal growth and characterization were supported by the ARO MURI on topological insulators (contract W911NF-12-1-0461), and by the US National Science Foundation (grant DMR 1420541). The high-field

experiments were performed at both the National High Magnetic Field Lab. NHMFL (Tallahassee) and at the Pulsed Field Facility (Los Alamos National Laboratory). NHMFL is supported by the National Science Foundation Cooperative Agreement no. DMR-1157490, the State of Florida and the US Department of Energy. The theory work was supported by grants to B.A.B. from the Department of Energy DE- SC0016239, Simons Investigator Award and NSF EAGER Award NOA - AWD1004957. B.S. is supported by the NSF STC 'Center for Integrated Quantum Materials' under Cooperative Agreement no. DMR-1231319.

Author contributions

The experiment was planned by S.L., S.K., R.J.C., Z.W., B.A.B. and N.P.O. S.L. led the measurement effort with assistance from T.G. and M.H. The crystals were grown and characterized by S.K., K.S. and R.J.C. Theoretical support was provided by J.L., Z.W., B.A.B. and B.S. The manuscript was written by N.P.O. with contributions from all authors.

Competing interests

The authors declare no competing interests.

Additional information

Supplementary information is available for this paper at https://doi.org/10.1038/s41563-019-0303-x.

Reprints and permissions information is available at www.nature.com/reprints.

Correspondence and requests for materials should be addressed to N.P.O.

Publisher's note: Springer Nature remains neutral with regard to jurisdictional claims in published maps and institutional affiliations.

Methods

Crystals of KHgSb were grown by slow cooling of a stoichiometric melt in vacuum-sealed quartz tubes from 700 °C. The required amounts of high-purity K, Hg and Sb (and Bi) were sealed in a thick-walled quartz tube. The ampoule was heated to 300 °C at the rate of 60 °C h^{-1}, annealed for 12 h and then heated to 650 °C again at the rate 60 °C h^{-1} for 12 h. As a last step, the temperature was raised to 700 °C at the same rate for 12 h. The hot ampoule was stirred to ensure a homogeneous molten mixture. The ampoule was slowly cooled to 300 °C at the rate 6 °C h^{-1} and annealed for 24 h, and finally cooled to room temperature at the rate 60 °C h^{-1}.

The ampoule was opened in an Ar-filled dry box to avoid exposure of the crystals to oxygen and moisture. The crystals, dark green in colour with large and shiny facets up to ~5 mm on a side, were cleavable along different crystallographic planes. The $D^4_{6h}(P6_3/mmc)$ phase of KHgSb was confirmed by single-crystal X-ray diffraction, as was the relationship between unit-cell axis directions and crystal morphology. The powder X-ray diffraction pattern on ground crystals was recorded by covering with a layer of Paratone-N oil followed by a layer of Kapton foil. A Le Bail fit was performed to the recorded diffraction pattern. The crystallographic cell parameters were found to be $a = 4.785$ Å and $c = 10.226$ Å. Doping with Bi (1–2%) was performed to lower the bulk carrier density n.

As a result of the high K content, crystals of KHgSb oxidize rapidly (within 30 s) on exposure to moist air. Hence, all manipulations and contacting with wires were carried out in an Ar-filled dry-box. The crystals were mounted inside a small capsule that was hermetically sealed with a cap (the capsule and cap are made of brass or G10 epoxy). Electrical wires were brought from the outside into the capsule through feed-through perforations at the bottom. Stycast epoxy was used to make the perforations gas-tight. After the electrical leads were contacted to the crystal with silver paint, the brass cap was screwed on tightly inside the argon dry-box. Indium solder was employed to achieve a hermetic seal. With this set up, samples are well protected against oxidation for up to a week. (For pulsed field experiments, the samples were sealed in G10 capsules to avoid eddy-current heating.)

Supplementary Fig. 1 shows the in-plane resistivity ρ_a measured in samples A4 (blue curve) and B1 (red curve) versus T. The large disorder arising from Hg vacancies leads to a profile that is T independent in A4. In B1 (with a carrier density 4× smaller than in A4), ρ_a displays an increase below 40 K. The sharp transitions at 4 K arise from surface superconductivity due to exuded Hg ions. The inset shows a photograph of a mounted crystal of KHgSb.

In the Hall experiments in pulsed fields, we first performed measurements of the Hall voltage V_H with the pulsed field direction **B** in the 'up' direction. After a wait-period of 50 min (to let the magnet coils cool back to liquid N_2 temperature), we performed a second measurement of V_H with **B** reversed. The long wait period between pulses gives rise to a spurious background offset δV_H that adds a small B-independent error signal to the inferred ρ_{yx}. We believe that δV_H is caused by very small temperature drifts during the wait period. This shift is not a major problem in most Hall experiments. Here, however, it gives a noticeable error when ρ_{yx} approaches zero and is exponentially sensitive to tiny changes in T. The offset can be seen in the trace of ρ_{yx} at 1.53 K in Fig. 2b of the main text. Analysis of the pulsed-field data was performed after this background is removed. We emphasize that in d.c. experiments (on batch B samples) this spurious background is absent.

Despite the hermetic seal, a particular sample cannot be re-used for a second round of experiments after it has been warmed from 4 K to room temperature and the cap re-opened (even inside an argon dry-box). The thermal cycling probably causes more Hg ions to be exuded to the surface and further oxidation due to a very small amount of residual water vapour inside the dry-box. To overcome this experimental difficulty, we typically prepare 6–10 encapsulated crystals for each run in the Pulsed Field Facility.

Data availability

All of the data displayed in the main text and Supplementary Information are available from S.H.L. (sihangl@princeton.edu) or N.P.O. (npo@princeton.edu) upon request.